# Understanding galvanic replacement reactions: the case of Pt and Ag

F. Merkoçi [a], J. Patarroyo [a, b], L. Russo [a, b], J. Piella [a, b], A. Genç [a, c], J. Arbiol [a, d], N.G. Bastús [a, **], V. Puntes [a, d, e, *]

[a] Institut Català de Nanociència i Nanotecnologia (ICN2), CSIC and BIST, Campus UAB, Bellaterra, 08193, Barcelona, Catalonia, Spain
[b] Universitat Autònoma de Barcelona (UAB), Campus UAB, 08193, Bellaterra, Barcelona, Catalonia, Spain
[c] Department of Metallurgy and Materials Engineering, Faculty of Engineering, Bartin University, 74100, Bartin, Turkey
[d] ICREA, Pg. Lluís Companys 23, 08010, Barcelona, Catalonia, Spain
[e] Vall d'Hebron Institut de Recerca (VHIR), 08035, Barcelona, Catalonia, Spain

## ARTICLE INFO

## ABSTRACT

Synthesis of nanocrystals (NCs), where material science elements are addressed with organic chemistry precision techniques, is especially challenging and difficult to control. This difficulty arises from the increased complexity of the mineralization processes and the generation of a liquid-solid interface. These aspects, along with a strong susceptibility to reaction kinetics, ultimately translate into serious challenges for reproducibility and morphological control. By systematically varying the different parameters used to control the morphology of NCs, including complexing agents, coreducers, and cooxidants, the general reaction landscape can be mapped and the most stable and reproducible recipes can be identified. We apply this concept to the model transmetallation reaction between immiscible Pt and Ag forming hollow Pt NCs by galvanic replacement reactions. In this work, 648 synthetic recipes were performed and characterized per duplicate, from which a subset of 307 recipes leading to the controlled formation of hollow NCs were further analyzed to correlate reaction conditions with the final obtained structure and stability (reproducibility). As a result, we present robust general synthetic protocols leading to the *ad hoc* production of Pt-based hollow NCs with independent control of shell thickness, void size, surface roughness, and degree of porosity.

© 2019 The Authors. Published by Elsevier Ltd. This is an open access article under the CC BY-NC-ND license (http://creativecommons.org/licenses/by-nc-nd/4.0/).

## 1. Introduction

The process of carving voids into nanocrystals (NCs) as the basis of a new generation of advanced functional materials [1,2] with outstanding properties [3–5] was initially described as a combination of galvanic replacement and nano-Kirkendall effects [1,6,7]. This approach includes a transmetallation process driven by the redox reaction between a colloidal suspension of preformed NCs — templates — and the cationic precursor of a more noble metal. The reduction of the noble metal cation is confined to the vicinity of the template surface, nucleating onto it, and then growing and forming an alloyed shell around it. During the more noble metal deposition, the original NC is simultaneously oxidized and dissolved through formed pinholes, resulting in hollow bimetallic structures. As the reaction proceeds, further corrosion processes promote the dealloying of the formed shell, generating multiple pores, leading to the formation of nanocages and nanoframes, which ultimately fragment and collapse into small (<5 nm) metal NC debris [1,8].

This picture, however, fails to fully describe the ensemble of experimental results that have been puzzling scientists since the seminal work of Xia et al [6]. Observations suggest that a hollowing process cannot be fully explained by a simple combination of galvanic replacement reactions [6] and vacancies coalescence — kirkendall effect — [7] because mass and charge balance between metal atoms and cations cannot fully explain the formed nanostructures [9]. Consequently, the mechanistic understanding of galvanic replacement in fabricating hollow bimetallic nanostructures has been discussed for years [8]. It is accepted that the reaction product is determined by a set of thermodynamic and kinetic parameters that are intimately and intricately entangled to each other. While the essence of thermodynamic control is to minimize the total free energy of a system, the manipulation of the deposition/dissolution rates allows trapping the system in thermodynamically unstable, but kinetically enabled state [10].

* Corresponding author.
** Corresponding author.
E-mail addresses: neus.bastus@icn2.cat (N.G. Bastús), victor.puntes@icn2.cat (V. Puntes).

Advanced electron microscopy characterization [11,12] and quantitative microanalysis [13] have been fundamental to thoroughly investigate intermediate and final NC states. Thus, researchers in the field have studied the effect of thermodynamic factors such as the surface free energies of template facets [14] and kinetic factors such as precursor reduction rate, atom diffusion coefficients, degree of alloying, and surface passivation, all strongly affecting the morphology of the resulting shells [15−17].

Despite the effort, the actual control of the different hollow morphologies has proved to be difficult. Owing to the fact that these colloidal systems are highly degenerated and that the energy barrier separating one morphology from another is relatively low [18], similar recipes may direct NC growth toward very different morphologies, whereas disparate synthetic recipes may lead to similar NCs [1,18,19]. These difficulties also account for the common problems of reproducibility systematically found in the scientific literature [20−22].

Herein, we systematically study the influence of the different synthetic parameters identified in the literature, including reaction temperature and time [11], metal template to precursor ratio [23], presence of cosurfactants [1,24], coreducing agents [25], ionic species [24], and order of reagent addition [24], on the final NC morphology. The study focuses on the particular case of PtAg because of the well-described limitations in the control of NC final morphology attributed to the poor miscibility between Ag and Pt at low temperatures (3.5% lattice mismatch) [24], which results in rough polycrystalline hollow NCs composed of small Pt domains as witness of a Volmer-Weber type of growth [8,26], which would not be the most desired for catalysis [27]. This study allows observing the role of the different constituents of the reaction. As a result, robust and reproducible general synthetic protocols leading to the *ad hoc* production of Pt-based hollow NCs with controlled shell thickness, void size, porosity, and surface roughness are presented. Indeed, this approach not only delivers rational synthetic pathways leading to particularly desired morphologies but also allows unsuccessful preparations to be explained, providing thus concepts and strategies to address 'failed' recipes.

## 2. Results and discussion

In our process of tailoring the hollowing process of PtAg bimetallic NCs, several chemical players crucially involved coexist: the Pt precursor − totally or partially reduced − the Ag template and oxidized $Ag^+$, the surfactant polyvinylpyrrolidone (PVP), acids in the form of HCl or $HNO_3$, halides − normally coming from the precursor − such as Cl or Br, and dissolved oxygen (DO) present in the reaction media. These different reagents are involved in two main tasks: (i) the reduction and deposition of a Pt shell onto the Ag surface and (ii) the oxidation and dissolution of the Ag template, which drives the creation of the hollow structure. Reducing species include metallic $Ag^0$ and PVP, while oxidizing species comprise the Pt precursor, $H_3O^+$, and the DO present in the media together with nucleophilic species, such as halides, which assist the oxidative corrosion of the Ag template (Fig. 1).

To address this issue, we systematically varied the aforementioned different synthetic parameters thereby generating multiple synthetic conditions schematically described in Fig. 2A. Accordingly, the hollowing process is not only controlled by an exchange of electrons between Ag and Pt but also affected by other agents that interfere in the PtAg redox process, creating more or less stable intermediates and driving equilibrium toward different products. In detail, 50 nm silver nanocrystals (Ag NC) sacrificial templates ($[Ag^0] = 0.25$ mM) were incubated with PVP at different $Ag^0$ to PVP molar ratios (0, 0.1 and 10), with the aim of varying their surface state (passivation) degree. For each condition described previously, the amount of $Pt^{2+}$ precursor was systematically adjusted with respect to that of $Ag^0$, from substoichiometric (0.25:1) to stoichiometric (1:1) and suprastoichiometric (10:1) molar concentrations. In addition, for each sample, a study on the effect of the type of etcher present in the reaction media (HCl, $HNO_3$, NaCl) and its relative molar concentration (0, 1, 10, and 100) with respect to that of $Ag^0$ was carried out. Finally, the reaction was performed at two different temperatures (room temperature [RT] and 90 °C) and characterized at three different reaction times (0.5, 4, and 24 h) as shown in Fig. 2B. A detailed description of the experimental procedure is provided in the supplementary information section.

The systematic variation of these synthetic parameters generated a collection of 648 experimental conditions, which were performed and characterized per duplicate. Among the explored conditions, not all of them were successful in terms of well-defined morphologies, monodispersity, and high product yield. As a result, these NC recipes were not further considered. Besides, we were able to identify a subset of 307 recipes that consistently led to a reduced number of Pt-based hollow NC morphology types (Fig. 2C), some of which have never been previously reported.

Representative transmission electron microscopy (TEM) images of the different morphologies are presented in Fig. 3. Their correlation with the synthetic parameters involved in their synthesis (Fig. 2A) allows concluding that rough and rather thick are the most common structures, whereas thin and smooth surfaces are rarer. It is important to note that among the different morphologies, those presenting smooth, thin, and porous shells are particularly attractive for catalysis because rough surfaces are more atomically relaxed than smooth ones [27]. In addition, thin shells imply less usage of Pt and porous structures maximize available surface, which account in part for their reported higher catalytic performance per gram [27−29]. Details of the synthesis procedure and an extended characterization of each individual Fig. 2 recipe and morphology are reported in the SI, section 2.2.

Regarding the smooth and thin NCs, they are obtained when (i) a high concentration of PVP promotes the protection (passivation) of the surface of the Ag NC templates along with the stabilization of the Pt ions by forming Pt-PVP complexes [30]; (ii) a progressive slow delivery of Pt precursor allows for the progressive reduction and deposition of Pt ions at low stoichiometric ratios; and (iii) the presence of a secondary etcher promotes the dissolution of the Ag atoms not corroded by the small amount of deposited Pt. Note that acids are also used to chemically cure the template surface by dissolving the less reactive $Ag_2O$ domains present at the working pH [31]. Furthermore, the presence of halides, as provided by $K_2PtCl_4$, HCl, or NaCl, favors the formation of AgCl domains onto the templates surface, acting as a physical protective barrier which is later exfoliated and solubilized by PVP (see SI, section 2.3) [1]. Halide ions, as nucleophilic species, also promote the oxidative corrosion of Ag in the presence of dissolved oxygen which, unless removed, is present in the reaction solution at significant concentrations at RT (3−9 mg/L) [32], as control experiments show (see SI, section 2.4). Performing the reaction at room temperature, instead of the original 100 °C [6], allows adjusting the reaction rate and hence promotes a relatively slow corrosion process favoring the formation of thin smooth surfaces, indicating again the importance of kinetic control. Finally, relatively short reaction times -few hours-are preferred to prevent PVP acting as a Pt reducer and inducing Pt shell overgrowth (even without the Ag NC template consumption), as shown in control experiments (see SI, section 2.5).

Thus, by adjusting these synthetic parameters, the controlled formation of thinner or thicker shells, with more or fewer pores, and bigger or smaller voids, can be independently achieved. It is worth pointing out that porous morphologies are generally not the predominant ones because the thickness of the shell limits the extent of the dealloying processes needed for the formation of pores [11,21].
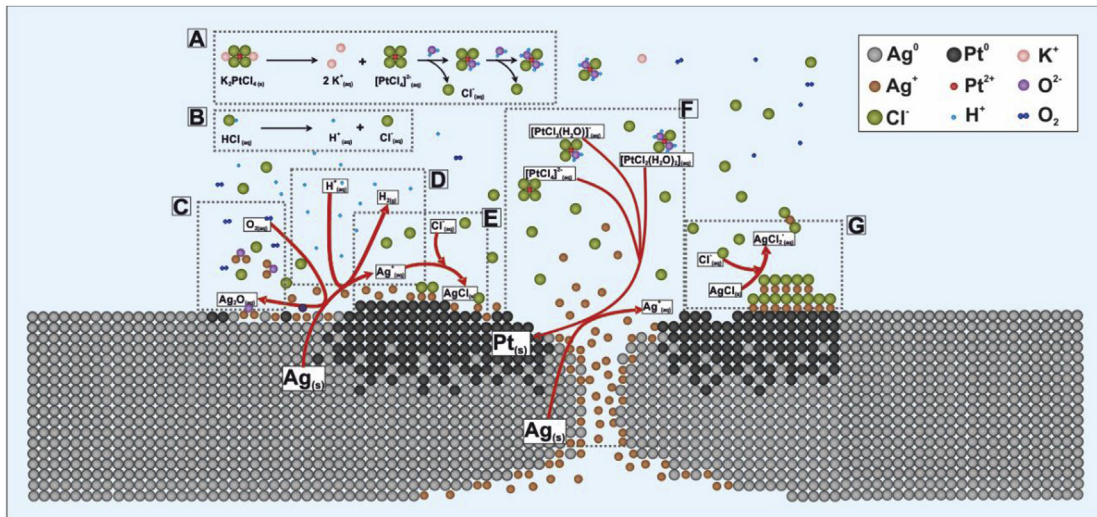
**Fig. 1. Map of competitive reactions**. Representation of the chemical processes running in parallel during a typical hollowing process. In detail, speciation of the Pt precursor (A) and HCl (B), formation of Ag$_2$O by the dissolved oxygen in the media (C), oxidation of Ag and dissolution of Ag$_2$O by H+ (D), formation of AgCl (E), galvanic replacement reaction between Ag and several different Pt species (F), and dissolution of AgCl (G).
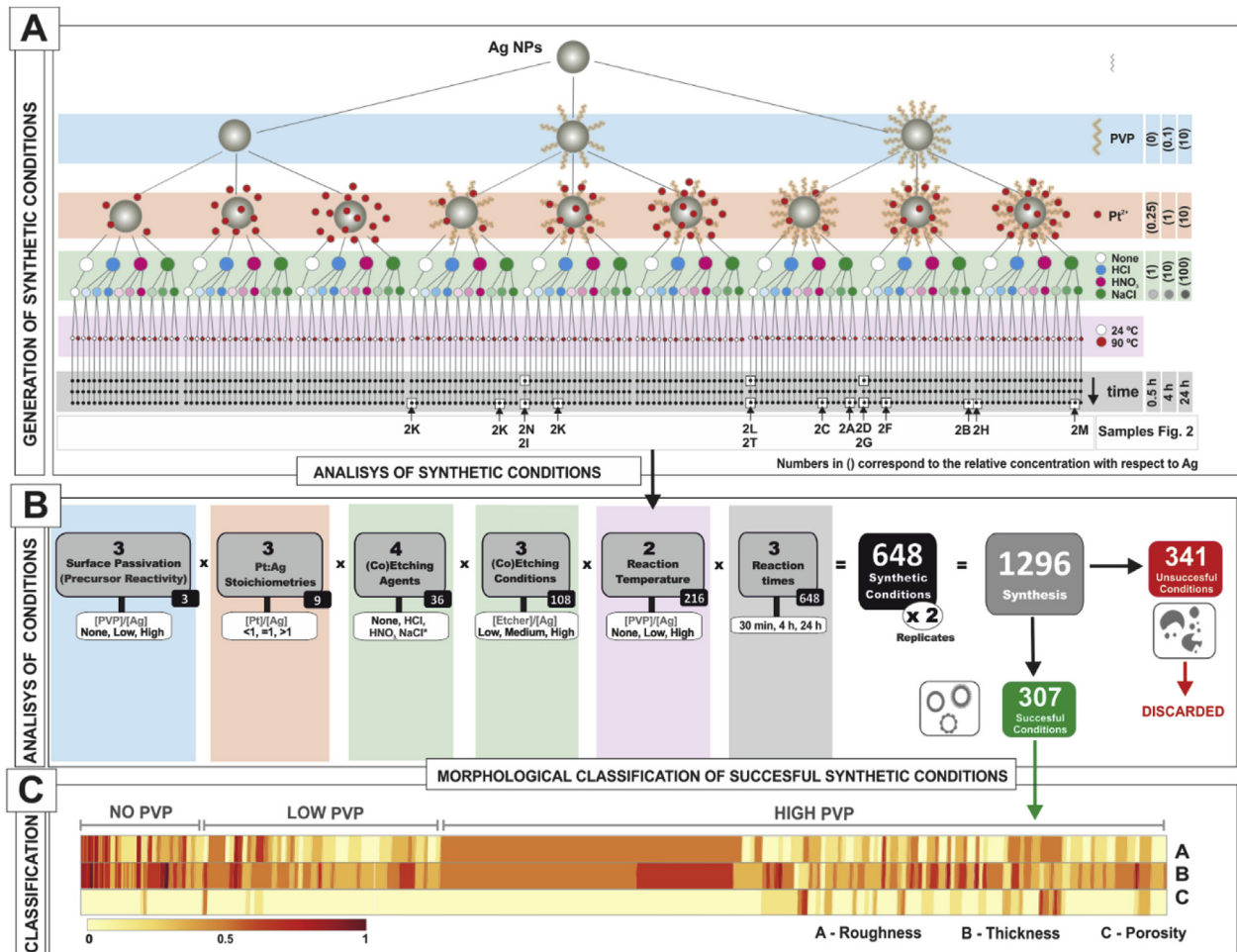


**Fig. 2. A systemic approach to NC synthesis**. A) Explored experimental conditions for the performed syntheses including 3 PVP concentrations, 3 Pt precursor concentrations, 4 different types of coetching agents each one at 3 different concentrations, 2 reaction temperatures, and 3 reaction times. The particular synthetic routes for the Pt-based hollow NCs displayed in Fig. 2 are explicitly indicated. (B) Analysis of synthetic conditions, for a total number of 648 different experimental conditions, which, tested per duplicate, leads to a total of 1296 synthesis. From these syntheses, only 307 recipes lead to the successful production of NCs in terms of well-defined morphologies, monodispersity, and high yield while the other 341 unsuccessful were discarded. (C) Morphological heatmap correlating the effect of PVP concentration with the degree of roughness, thickness, and porosity of 307 syntheses. (Every single line corresponds to a unique synthesis.) The color scale varies from yellow (low values) to deep red (high values). PVP = polyvinylpyrrolidone, NCs = nanocrystals.
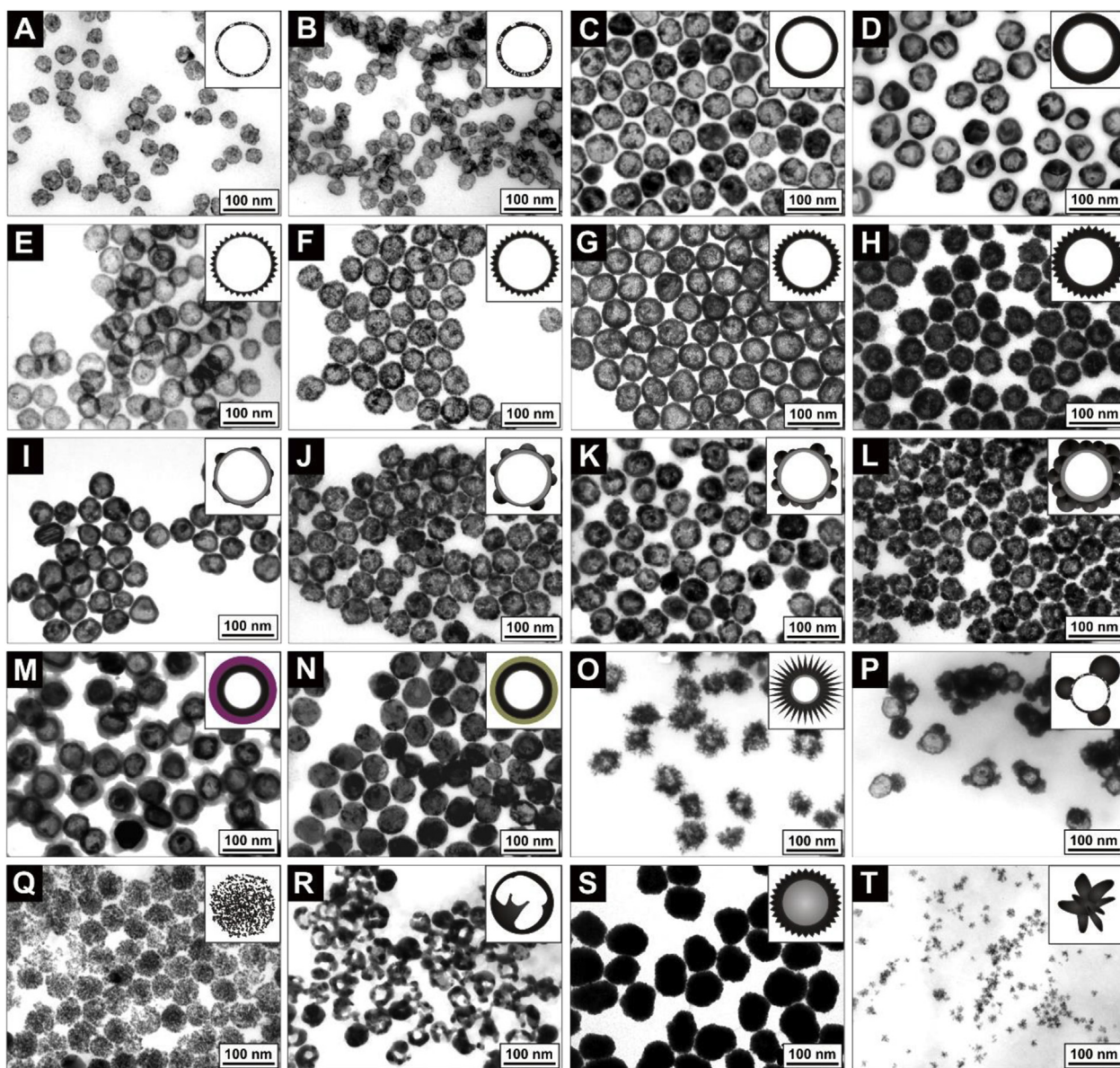
**Fig. 3. Representative TEM images of Pt-based hollow NCs obtained**. Collection of TEM images of Pt-based hollow NCs with different degrees of shell morphology and thickness showing (A−D) smooth, (E−H) rough, (I−L) popcorn-like rough surfaces, and more complex morphologies such as (M) PtHollow@PtCl$_2$ Core@Shell NCs, (N) PtHollow@AgCl Core@Shell NCs, (O) urchin-like Pt hollow NCs, (P) Pt heterostructures with hollow domains, (Q) highly porous Pt NCs, (R) Pt nanoshells, (S) Ag@Pt Core@Shell NCs, and (T) Pt nanostars. For clarity, upper right panels show a representation of an individual particle. TEM = transmission electron microscopy, NC = nanocrystals.

This is shown schematically in Fig. 4, where a simplified representation of the two major synthetic pathways governing this process is presented (Fig. 4A). The first case, the 'high reactivity route', is the synthesis with non-passivated templates and/or non-complexed Pt species. The addition of either the Pt precursor or a combination of both Pt precursor and acids yields thick and rough shells, characteristic of the island-mode of growth of Pt onto Ag. When exposed to further etching processes -for instance, HCl, HNO₃, or NaCl- and depending on the thickness of the shell, the dissolution of the remaining (unreacted) Ag atoms leads to broken Pt shells before the dealloying can be controlled. In the second case, the 'low reactivity route' performing the synthesis with passivated Ag NCs and/or complexed Pt species leads to smooth-surface structures that can be controllably thinned and dealloyed yielding nanocages. If this process is conducted in the absence of acids or deoxygenated water, higher quantities of the Pt precursor are needed to completely oxidize the Ag templates, promoting the formation of thicker Pt shells and, therefore, fewer pores. Conversely, when performing the synthesis in presence of etchers, owing to the cooxidation process, a lesser amount of Pt precursor is needed to consume the Ag templates, allowing the template's voiding stoichiometry to change. This is ultimately translated into the formation of thinner Pt shells that are easier to dealloy and, therefore, multiple pores can be generated, as shown in Fig. 4B.

Summarizing, these results clearly indicate that Pt shell thickness and its morphology are two characteristics that can be controlled independently. Thinner shells are obtained by the sum of two different conditions:( i) minimum Pt layer growth using small amounts of Pt precursors and ii) maximum voiding (etching) of the core using cooxidants. Moreover, surface roughness can be controlled by lowering the reactivity of both the Pt precursors and the Ag templates, using surfactants to complex precursors and to absorb onto NC surfaces. Porous structures are easier to obtain when the thickness of the shell is relatively thin and the etchant can easily reach the unreacted Ag atoms bound to Pt.

To facilitate the comparison of event probability, morphological heatmaps were generated by classifying the samples according to their morphological characteri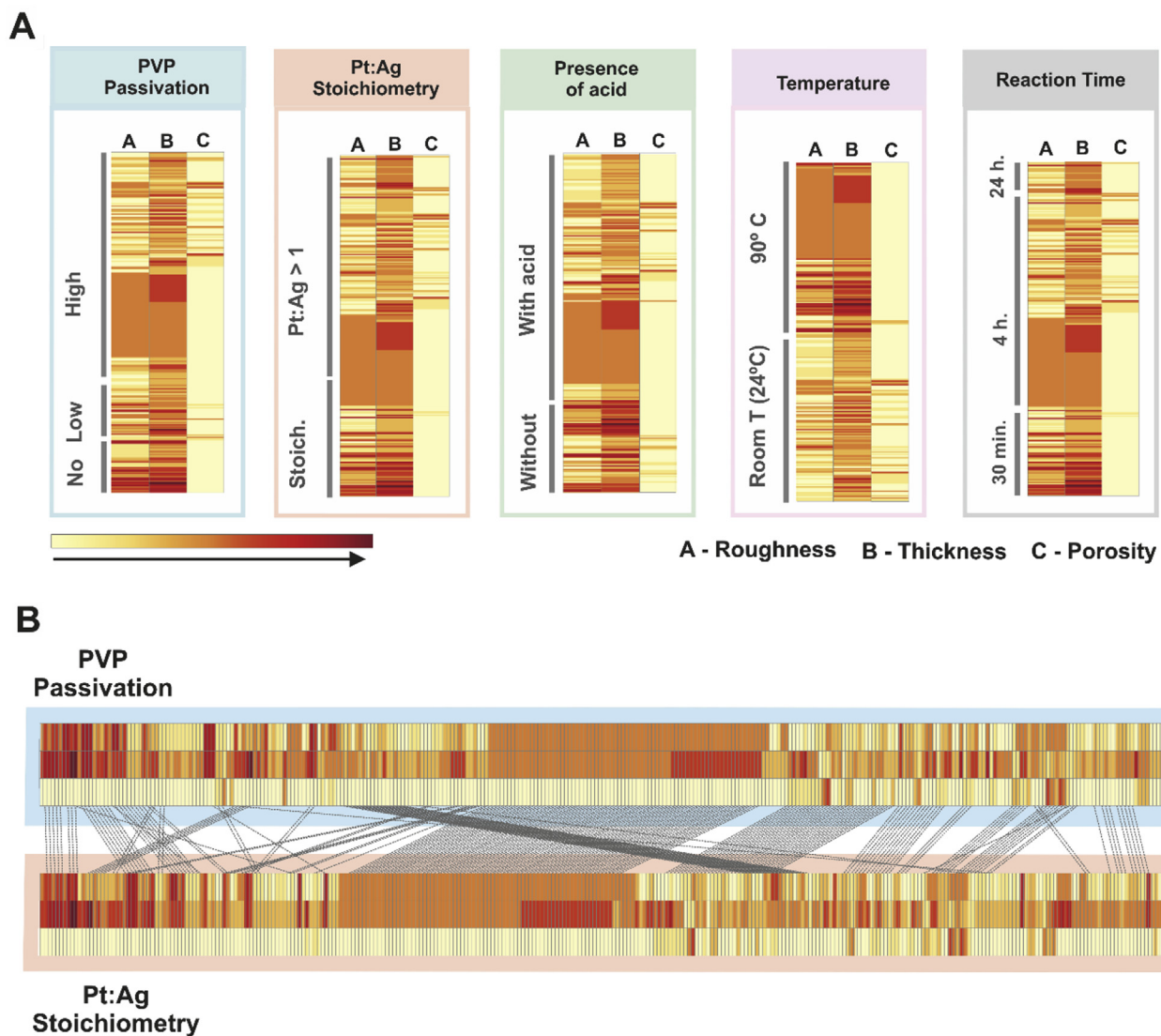stics – roughness, thickness, and porosity – considering the experimental conditions of each experiment. Morphological features were extracted from the characterization data of all the experiments, further analyzed using Image J. Standard distribution and the respective standard deviations were determined by measuring 150 to 900 particles of each condition. The relative roughness, the shell thickness, and the relative porosity were geometrically estimated (materials and methods and S.I.). The results were grouped in the diagrams shown in Fig. 5. The dominance of warmer lines in the heatmaps indicates a natural tendency of the system to form structures with rough surfaces and thick shells (>5 nm) with a low degree of porosity. This is as a consequence of the Pt-Ag immiscibility [26], and the preference for the Volmer-Weber type of growth, which is translated in the well-known synthetic limitations in the production of ultrathin Pt-based hollow NCs with Ag templates [28]. In contrast, less abundant lighter lines of thinner and smoother shells generally appear in conditions where chemical potentials are reduced [1].

In these diagrams (Fig. 5A), one can observe different features. First, a large orange area is always present rather centered – except for temperature – indicating that at these middle conditions the system is less degenerated and hence reproducibility is easier to achieve, and monodispersity high, yielding NCs which are not very thin, not very smooth, and not very porous. As soon as one goes to more extreme conditions, excess or lack of the reagent and/or reaction time, the system becomes more unstable and thin red and light lines intercalate, allowing for different structures at the expense of less reproducibility and morphological control. The only diverging graph is with temperature (T), where stability and reproducibility are achieved at higher T, yielding thick rough NCs. In this situation, the morphological possibilities are further limited. Note that initially, the hollowing process was described at high T, for the evident reasons shown here. However, when we decreased T, we acceded to more kinetic control and consequently, morphological control [1].

By comparing individual morphological heatmaps, the stability zones of the different synthetic parameters can be correlated. For example, by comparing the heatmaps of PVP passivation and Pt:Ag
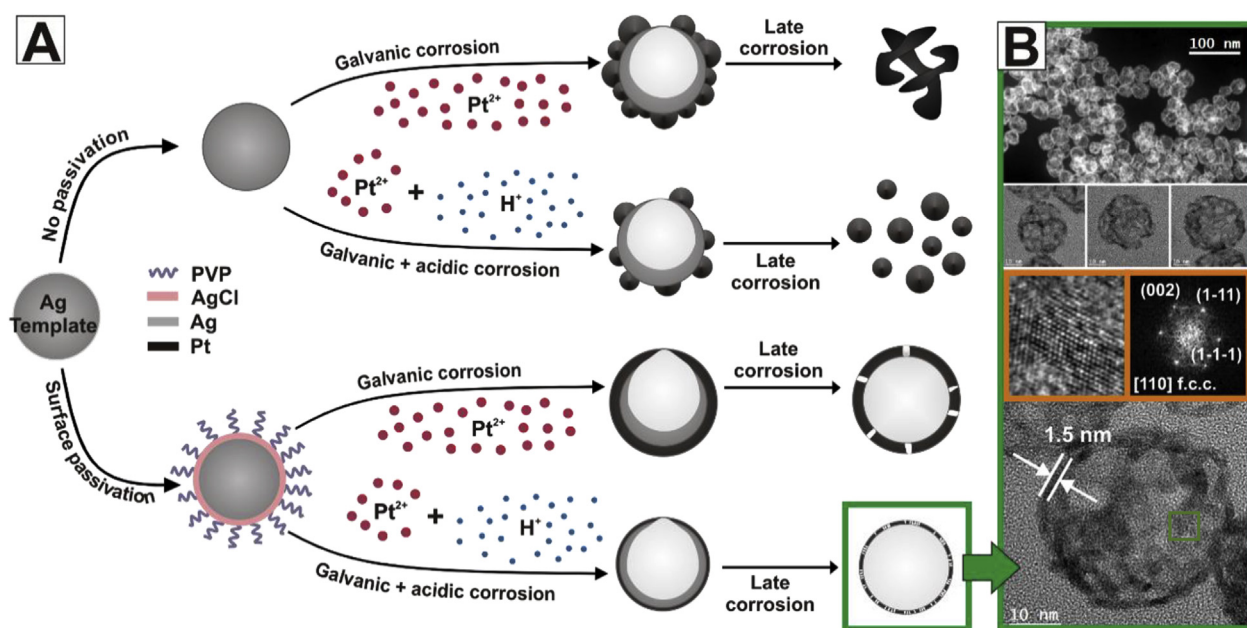


Fig. 4. Schematic representation of principal synthetic pathways governing the synthesis of Pt-based hollow NCs. (A) Representation of the synthetic pathways to produce distinct types of Pt-based hollow NCs. A detailed characterization of the thinnest shell case is shown in (B), where upper panels show low magnification HAADF-(S)TEM and bright-field TEM micrographs of individual particles and the lower panel shows an HRTEM image of a representative individual particle with details of the orange squared region and its corresponding power spectrum. TEM = transmission electron microscopy, NCs = nanocrystals, HAADF = high-angle annular dark-field imaging, STEM = scanning transmission electron microscopy, HRTEM = high-resolution transmission electron microscopy

**Fig. 5. Morphological Susceptibility heatmaps**. (A) Morphological heatmaps correlating the effect of the synthetic parameters explored with the degree of roughness, thickness, and porosity of more than 300 syntheses. (B) Comparison of two individual morphological heatmaps shown in Fig. 4, where the stability zones of the different synthetic parameters can be correlated and the overall reproducibility of the synthesis can be identified. Colors represent the conditions tested as shown in Fig. 1. Every single line corresponds to a unique synthesis.

stoichiometry, a central crossing area between the two diagrams is observed (Fig. 5B). This indicates that similar results can be obtained either by increasing the PVP concentration or decreasing the $Pt^{2+}$ amount, two different manners of decreasing chemical potential. This relationship is lost in the extremes of the graphs where the recipes become less robust.

In summary, by systematically modifying reagents and coreagents, great morphological control is achieved in the challenging PtAg system. Six hundred forty-eight synthetic recipes were explored from which a subset of more than 307 where further analyzed to correlate the presence of different ingredients at different temperatures and times with the final obtained morphology. Our data demonstrate that the Ag NC voiding and Pt shell growing processes can be independently controlled, which allows for the design of *ad hoc* recipes for future intended morphologies and, at the same time, an understanding of the mechanism behind synthetic failures. The presented systemic approach to NC syntheses may be extended to other general strategies for the mineralization of ions in solution controlled by organic reactants and surfactants for the production of advanced NCs [2].

## Materials and methods

### Chemicals

Silver nitrate (SN, AgNO₃) ReagentPlus, trisodium citrate (SC, $Na_3C_6H_5O_7$), tannic acid (TA, $C_{76}H_{52}O_{46}$), polyvinylpyrrolidone (PVP, molecular weight = 55,000 g/mol), and Potassium tetrachloroplatinate (II) ($K_2PtCl_4$) were purchased from Sigma-Aldrich. All reagents were used as received without further purification. Distilled water passed through a Millipore system ($\rho$ = 18.2 MΩ) was used in all experiments.

### Synthesis of silver nanocrystals

Silver nanocrystals of ~50 nm in diameter were prepared by the seeded growth method recently reported by Bastús et al. [33]. In a typical experiment, silver seeds were obtained by filling a three-neck round-bottomed flask with a 100 mL aqueous solution containing 5 mM sodium citrate (SC) and 0.1 mM of tannic acid (TA) and heated up with a heating mantle up to 100 °C. After boiling had commenced, 1 mL of 25 mM AgNO₃ was injected into this solution under vigorous stir. The as-obtained silver seeds were grown by cooling down the solution to 90 °C and sequentially injecting 100 μL of 25 mM SC, 250 μL of 2.5 mM TA, and 250 μL of 25 mM AgNO₃. This process was repeated up to four times. In the same vessel, the seed solution was diluted by extracting 20 mL of sample and adding 17 mL of Milli-Q water, then 500 μL of 25 mM SC, 1.5 mL of 2.5 mM TA, and 1 mL of 25 mM AgNO3 were sequentially injected, again. This process was repeated up to 5 times, progressively growing the size of the Ag NCs until reaching the desired size (~50 nm). The obtained Ag NCs were purified by centrifugation and stored in either water, PVP, or in a solution containing both TA and SC. See detailed characterization in SI, section 2.1.

### Synthesis of Pt-based hollow nanocrystals

To standardize all of our experiments, the synthesis consisted of firstly preparing a 1.5 mL aqueous solution containing all the explored reagents at different concentrations into which 0.5 mL of the Ag NCs (1 mM) were rapidly added (for a total 2 mL volume) to let the reactions begin. Each reaction was conducted for a specific time, at a specific temperature under vigorous stirring. In detail, the standard volumes used were 1 mL of PVP (either 0, 0.05, or 5 mM corresponding to a PVP to Ag ratio of 0, 0.1, and 20, respectively); 250 μL of $K_2PtCl_4$ (either 0.25, 1, or 10 mM, which, according to the $Pt^{2+}$ vs Ag redox stoichiometry correspond to a Pt to Ag ratios of 0.25, 1, or 10 mM, respectively); and 250 μL of etchant solution which was either HCl, HNO₃, NaCl or the correspondent controls with water (each one of them at three different concentrations: 2, 20, and 200 mM corresponding to an etchant to Ag ratio of 1, 10, and 100, respectively).

### Electron microscopy characterization

Before the inspection, samples were precipitated and redispersed in water several times for their purification. After sonicating the samples for 5 min, the solution was dropcasted onto a Formvar-coated 200-mesh copper grid (Ted.Pella, Inc.) and left drying at room temperature overnight. TEM images were obtained using an 80 keV TEM (Jeol 1010, Japan) and high-resolution transmission electron microscopy (HRTEM) and Scanning transmission electron microscopy (STEM)/ high-angle annular dark-field imaging (HAADF) images were obtained in an FEI Tecnai G2 F20 S-TWIN HR(S) TEM, operated at an accelerated voltage of 200 kV.

### Morphological heatmaps

Morphological heatmaps were generated using the characterization data of all the experiments, which were analyzed with Image J. The statistical distribution and the respective standard deviations were determined by measuring 150 to 900 particles. In detail, the RR, the ST, and the RP of the Pt-based hollow nanocrystals (shown in Fig. 3) was geometrically estimated as follows: For the RR, the cross-section of more than 150 particles was integrated in comparison with their idealistic cross-section (which corresponds to the minimum radius described inside the real cross-section), as schematically shown in Scheme S1. The values of the ratios between the real and the ideal cross-section ranged from 1.0 to 2.2 in all the cases. Therefore the 'perfectly smooth' particles were assigned to the minimum ratio (1.0) and the 'highly rough' ones to the maximum one (2.2). The obtained values were further normalized between [0, 1]. The RP was similarly estimated by counting the number of pores in the perimeter of the cross-section. The values obtained ranged from 0.0 (non-porous particles) to 23 (highly porous particles) and were also normalized between [0, 1]. Finally, the ST was conventionally measured by using Image J and the values obtained ranged from 1.5 nm (minimum thickness) to 14.4 nm (maximum thickness) and, as in the previous cases, were also normalized between [0, 1].

## Declaration of competing interest

The authors declare that they have no known competing financial interests or personal relationships that could have appeared to influence the work reported in this article.

## Acknowledgments

## Appendix A. Supplementary data

Supplementary data to this article can be found online at https://doi.org/10.1016/j.mtadv.2019.100037.

## References

[1] E. Gonzalez, J. Arbiol, V.F. Puntes, Carving at the nanoscale: sequential galvanic exchange and Kirkendall growth at room temperature, Science 334 (6061) (2011) 1377−1380.

[2] W.J. Parak, Materials science. Complex colloidal assembly, Science 334 (6061) (2011) 1359−1360.

[3] M.A. Mahmoud, F. Saira, M.A. El-Sayed, Experimental evidence for the nano-cage effect in catalysis with hollow nanoparticles, Nano Lett. 10 (9) (2010) 3764−3769.

[4] Z.W. Shan, G. Adesso, A. Cabot, M.P. Sherburne, S.A. Asif, O.L. Warren, D.C. Chrzan, A.M. Minor, A.P. Alivisatos, Ultrahigh stress and strain in hierarchically structured hollow nanoparticles, Nat. Mater. 7 (12) (2008) 947−952.

[5] A. Genç, J. Patarroyo, J. Sancho-Parramon, N.G. Bastús, V. Puntes, J. Arbiol, Hollow metal nanostructures for enhanced plasmonics: synthesis, local plasmonic properties and applications, Nanophotonics 6 (1) (2017) 193−213.

[6] Y. Sun, Y. Xia, Shape-controlled synthesis of gold and silver nanoparticles, Science 298 (5601) (2002) 2176−2179.

[7] Y. Yin, R.M. Rioux, C.K. Erdonmez, S. Hughes, G.A. Somorjai, A.P. Alivisatos, formation of hollow nanocrystals through the nanoscale Kirkendall effect, Science 304 (5671) (2004) 711−714.

[8] X. Xia, Y. Wang, A. Ruditskiy, Y. Xia, 25th anniversary article: galvanic replacement: a simple and versatile route to hollow nanostructures with tunable and well-controlled properties, Adv. Mater. 25 (44) (2013) 6313−6333.

[9] L.M. Moreau, C.A. Schurman, S. Kewalramani, M.M. Shahjamali, C.A. Mirkin, M.J. Bedzyk, How Ag nanospheres are transformed into AgAu nanocages, J. Am. Chem. Soc. 139 (35) (2017) 12291−12298.

[10] Y. Xia, X. Xia, H.-C. Peng, Shape-controlled synthesis of colloidal metal nanocrystals: thermodynamic versus kinetic products, J. Am. Chem. Soc. 137 (25) (2015) 7947−7966.

[11] B. Goris, L. Polavarapu, S. Bals, G. Van Tendeloo, L.M. Liz-Marzán, Monitoring galvanic replacement through three-dimensional morphological and chemical mapping, Nano Lett. 14 (6) (2014) 3220−3226.

[12] S.F. Tan, G. Lin, M. Bosman, U. Mirsaidov, C.A. Nijhuis, Real-time dynamics of galvanic replacement reactions of silver nanocubes and Au studied by liquid-cell transmission electron microscopy, ACS Nano 10 (8) (2016) 7689−7695.

[13] H. Jing, H. Wang, Structural evolution of Ag−Pd bimetallic nanoparticles through controlled galvanic replacement: effects of mild reducing agents, Chem. Mater. 27 (6) (2015) 2172−2180.

[14] C. Zhu, D. Du, A. Eychmüller, Y. Lin, Engineering ordered and nonordered porous noble metal nanostructures: synthesis, assembly, and their applications in electrochemistry, Chem. Rev. 115 (16) (2015) 8896−8943.

[15] S. Neretina, R.A. Hughes, K.D. Gilroy, M. Hajfathalian, Noble metal nanostructure synthesis at the liquid−substrate interface: new structures, new insights, and new possibilities, Acc. Chem. Res. 49 (10) (2016) 2243−2250.

[16] Y. Wu, X. Sun, Y. Yang, J. Li, Y. Zhang, D. Qin, Enriching silver nanocrystals with a second noble metal, Acc. Chem. Res. 50 (7) (2017) 1774−1784.

[17] K.D. Gilroy, A. Ruditskiy, H.-C. Peng, D. Qin, Y. Xia, Bimetallic nanocrystals: syntheses, properties, and applications, Chem. Rev. 116 (18) (2016) 10414−10472.

[18] S.I. Lim, I. Ojea-Jimenez, M. Varon, E. Casals, J. Arbiol, V. Puntes, Synthesis of platinum cubes, polypods, cuboctahedrons, and raspberries assisted by cobalt nanocrystals, Nano Lett. 10 (3) (2010) 964−973.

[19] S.I. Lim, M. Varón, I. Ojea-Jiménez, J. Arbiol, V. Puntes, Exploring the limitations of the use of competing reducers to control the morphology and composition of Pt and PtCo nanocrystals, Chem. Mater. 22 (15) (2010) 4495−4504.

[20] S. Adams, D. Thai, X. Mascona, A.M. Schwartzberg, J.Z. Zhang, Key factors affecting the reproducibility of synthesis and growth mechanism of near-infrared absorbing hollow gold nanospheres, Chem. Mater. 26 (23) (2014) 6805−6810.

[21] K.D. Gilroy, P. Farzinpour, A. Sundar, R.A. Hughes, S. Neretina, Sacrificial templates for galvanic replacement reactions: design criteria for the synthesis of pure Pt nanoshells with a smooth surface morphology, Chem. Mater. 26 (10) (2014) 3340−3347.

[22] D. Wan, X. Xia, Y. Wang, Y. Xia, Robust synthesis of gold cubic nanoframes through a combination of galvanic replacement, gold deposition, and silver dealloying, Small 9 (18) (2013) 3111−3117.

[23] A. Popa, A.C.S. Samia, Effect of metal precursor on the growth and electrochemical sensing properties of Pt-Ag nanoboxes, Chem. Commun. 50 (55) (2014) 7295−7298.

[24] W. Zhang, J. Yang, X. Lu, Tailoring galvanic replacement reaction for the preparation of Pt/Ag bimetallic hollow nanostructures with controlled number of voids, ACS Nano 6 (8) (2012) 7397−7405.

[25] H. Zhang, M. Jin, J. Wang, M.J. Kim, D. Yang, Y. Xia, Nanocrystals composed of alternating shells of Pd and Pt can Be obtained by sequentially adding different precursors, J. Am. Chem. Soc. 133 (27) (2011) 10422−10425.

[26] J. Chen, B. Wiley, J. McLellan, Y. Xiong, Z.Y. Li, Y. Xia, Optical properties of Pd-Ag and Pt-Ag nanoboxes synthesized via galvanic replacement reactions, Nano Lett. 5 (10) (2005) 2058−2062.

[27] E. González, F. Merkoçi, R. Arenal, J. Arbiol, J. Esteve, N.G. Bastús, V. Puntes, Enhanced reactivity of high-index surface platinum hollow nanocrystals, J. Mater. Chem. 4 (1) (2016) 200−208.

[28] L. Zhang, L.T. Roling, X. Wang, M. Vara, M. Chi, J. Liu, S.I. Choi, J. Park, J.A. Herron, Z. Xie, M. Mavrikakis, Y. Xia, Platinum-based nanocages with subnanometer-thick walls and well-defined, controllable facets, Science 349 (6246) (2015) 412−416.

[29] H. Zhang, M. Jin, H. Liu, J. Wang, M.J. Kim, D. Yang, Z. Xie, J. Liu, Y. Xia, Facile synthesis of Pd-Pt alloy nanocages and their enhanced performance for preferential oxidation of CO in excess hydrogen, ACS Nano 5 (10) (2011) 8212−8222.

[30] Y. Borodko, S.E. Habas, M. Koebel, P. Yang, H. Frei, G.A. Somorjai, Probing the interaction of poly(vinylpyrrolidone) with platinum nanocrystals by UV-Raman and FTIR, J. Phys. Chem. B 110 (46) (2006) 23052−23059.

[31] Y. Yang, J. Liu, Z.W. Fu, D. Qin, Galvanic replacement-free deposition of Au on Ag for core-shell nanocubes with enhanced chemical stability and SERS activity, J. Am. Chem. Soc. 136 (23) (2014) 8153−8156.

[32] H.A.C. Montgomery, N.S. Thom, A. Cockburn, Determination of dissolved oxygen by the winkler method and the solubility of oxygen in pure water and sea water, J. Appl. Chem. 14 (7) (2007) 280−296.

[33] N.G. Bastus, F. Merkoci, J. Piella, V. Puntes, Synthesis of highly monodisperse citrate-stabilized silver nanoparticles of up to 200 nm: kinetic control and catalytic properties, Chem. Mater. 26 (9) (2014) 2836−2846.